Accepted Manuscript

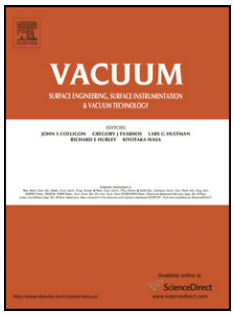

Design of 95 GHz, 100 kW Gyrotron for Active Denial System Application

Nitin Kumar, Udaybir Singh, Anil Kumar, A.K. Sinha

PII: S0042-207X(13)00151-6

DOI: 10.1016/j.vacuum.2013.05.002

Reference: VAC 6012

To appear in: *Vacuum*

Received Date: 17 January 2013

Revised Date: 30 April 2013

Accepted Date: 5 May 2013

Please cite this article as: Kumar N, Singh U, Kumar A, Sinha A, Design of 95 GHz, 100 kW Gyrotron for Active Denial System Application, *Vaccum* (2013), doi: 10.1016/j.vacuum.2013.05.002.

The main highlights of this paper are as following:

- Complete design of 95 GHz, 100 kW gyrotron is performed for Active Denial System application.
- The simulated results of interaction cavity by using PIC code are compared with the results of non-linear theory.
- The overall efficiency of the device is found around 50 %.

Design of 95 GHz, 100 kW Gyrotron for Active Denial System Application

Nitin Kumar, Udaybir Singh, Anil Kumar and AK Sinha
Central Electronics Engineering Research Institute, Pilani-333 031
(Council of Scientific and Industrial Research)
Email: nitingkv@gmail.com

Abstract – The design work of 95 GHz, 100 kW gyrotron for Active Denial System (ADS) application is reported in this manuscript. The mode selection is performed considering the various technical constraints. Particle-in-Cell code and indigenously developed code based on the generalized non-linear formalism are used in the beam-wave interaction computation and cavity design. Both the codes show good similarity in results. In addition, the design of electron beam source of 364 kW beam power, beam tunnel, depressed collector and RF window are also discussed. The design results confirm the RF power >100 kW with ≈50 % tube efficiency.

Keywords- Gyrotron, ADS system, beam-wave interaction, MIG, collector, RF window

1. INTRODUCTION

Gyrotron oscillators are high power sources of coherent millimeter wave and THz wave radiation based on the cyclotron resonance maser effect. An ultra high vacuum (< 10^{-8} torr) is required in these devices for the efficient transmission of electron beam and thus they are called vacuum electron devices. The fabrication as well as the design of these devices becomes complicated due to the presence of ultra high vacuum [1, 2]. These devices are widely used by the plasma fusion community in multi-megawatt long-pulse electron cyclotron heating and current drive (ECH&CD) in magnetic confinement fusion plasma devices [3, 4]. Recently, the significant progress is obtained in the research on megawatt class gyrotrons in frequency range 30-170 GHz due to the increasing demand in several ongoing plasma fusion activities, like, ITER, W7-X, JT-60, DIII-D, etc. During the last two decades, several other possibilities of gyrotron applications, such as material processing, THz spectroscopy, etc, were explored and the detail review can be found in Refs. [5-7]. A novel application of gyrotron is purposed recently in non lethal, counter personnel, directed energy weapon system also called Active Denial System (ADS) which can be used against human targets at a distance beyond the effective range of small arms [8]. 95 GHz radiation with 100 kW of power is suitable for ADS application due to the relative minimum of atmospheric absorption at 95 GHz [5,8,9]. Gyrotron is a very suitable device for the generation of 100 kW, 95 GHz radiation and is used in the current development of ADS system. The development of 95 GHz gyrotron for the US army ADS system is currently going on at Communication & Power Industry

(CPI) [10,11]. Here the design approach for 95 GHz gyrotron is slightly different as the combination of various indigenously developed and commercially available design codes is used effectively. The operating mode is also different from the mode used in CPI gyrotron.

The design and development of 95 GHz gyrotron is planned at CEERI, India considering the application in strategic area of ADS system. Here, the design results of this gyrotron are presented and discussed. The design goals and specifications of 95 GHz gyrotron are given in table 1. The design task is completed through the proper combination of indigenously developed and commercially available design codes. The description of the developed codes is given in the successive sections. Commercially available Particle-in-Cell (PIC) code MAGIC is used in the interaction cavity design and beam-wave interaction computation [12]. The beam-wave interaction analysis is also performed by using the self consistent nonlinear theory [13, 14]. A computer code based on the nonlinear formulation is developed to calculate the beam-wave interaction efficiency and discussed in section III. The beam-wave interaction results obtained in the PIC simulations show very good similarity with the nonlinear results. Further, the trajectory code EGUN is used in the design of electron gun and beam collector and discussed in sections IV and VI.

Table 1: Design specifications and goals

Frequency (f)	95 GHz
Power (P_{out})	100 kW
Beam current (I_b)	6-8 A
Beam voltage (V_b)	50-55 kV
Velocity ratio (α)	1.3-1.5
Total efficiency (η)	≈ 50%
Wall loss (dP/dA)	< 2 kW/cm^2
Voltage depression (V_d)	< 10% of V_b
Magnetic field at cavity (B_0)	3.55-3.57 T

2. MODE SELECTION AND COLD CAVITY ANALYSIS

The given frequency of 95 GHz corresponds to the wavelength (λ) of 3.156 mm. For the wavelength considered here, the cavity radius (R_c) and beam radius (R_b) are calculated by $R_c = \chi_{m,p}\lambda/2\pi$ and $R_b = \chi_{m\pm s,i}\lambda/2\pi$, respectively, where $\chi_{m,p}$ is the p^{th} root of m^{th} order first kind Bessel function derivative. First maxima (i=1) of the $TE_{m,p}$ mode for the beam launching and fundamental harmonic operation (s=1) are selected here, since these provide better coupling of the electron beam to the RF field. In the mode

selection process, the modes with eigenvalues ranging from 10 to 24 are explored. Various mode selection parameters such as space charge effect [15], ohmic wall loading [16], frequency separation from the most competing modes [17], etc, are calculated for all the considered modes by using in-house developed code GCOMS [18,19]. Further, various design and technical constraints (like voltage depression V_d, limiting current I_L, peak ohmic wall loading dP/dA, and support to the quasi optical mode launcher, etc) are applied to the considered modes through GCOMS. The qualified modes with the calculated mode selection parameters are given in table 2. For a $TE_{m,p}$ mode, the most dangerous competing modes are $TE_{(m-3),(p+1)}$ and $TE_{(m-1),p}$ and the frequency separation of the operating mode from these modes should be as large as possible [17]. The frequency separations ($\Delta f_1=[\chi_{m,p}-\chi_{(m-3),(p+1)}]/\chi_{m,p}\times100\%$ and $\Delta f_2=[\chi_{m,p}-\chi_{(m-1),p)}]/\chi_{m,p}\times100\%$) of the operating mode from these modes are also calculated and shown in table 2. Finally, $TE_{7,3}$ is selected as the operating mode as it satisfies all the mode selection parameters within limit (V_d<10% of V_b, $I_L>2I_b$, dP/dA<2 kW/cm^2) and the frequency separations from the most competing modes are also sufficient. The ohmic wall loading, shown in table 2, is for the cold copper with ideal smooth surface. Practically, the ohmic wall loading, considering the surface roughness and temperature dependence of material conductivity, can be taken twice of the ideal ohmic wall loading (0.231 kW/cm^2 for selected operating mode) [20]. Thus the real Ohmic wall loading for the designed interaction cavity is roughly 0.4-0.5 kW/cm^2, which is far below the technical limit of 2 kW/cm^2.

Table 2: Various calculated parameters for suitable TE modes

Mode	$\chi_{m,p}$	R_c **(mm)**	R_b **(mm)**	V_d **(kV)**	I_l **(A)**	dP/dA **(kW/cm^2)**	Δf_1 **(%)**	Δf_1 **(%)**
$TE_{8,3}$	17.774	8.93	4.289	0.91	34.68	0.203	2.593	7.4789
$TE_{9,3}$	19.004	9.55	4.851	0.84	37.55	0.180	2.361	6.472
$TE_{7,4}$	19.962	10.03	3.758	1.229	25.93	0.146	3.838	7.048
$TE_{7,3}$	16.444	8.25	3.758	0.986	32.295	0.231	2.947	7.486
$TE_{6,4}$	18.555	9.33	3.226	1.329	23.978	0.166	4.134	6.694
$TE_{6,3}$	15.213	7.65	3.220	1.08	29.493	0.262	4.131	8.061
$TE_{5,2}$	10.521	5.29	2.672	1.149	42.392	0.539	5.237	11.768
$TE_{10,4}$	23.762	11.94	5.384	1.34	36.323	0.100	1.919	5.303

The mode competition is a severe problem in the design of interaction cavity and it can be analyzed in number of ways explained in Refs. [21-23]. Here, the start oscillation current (SOC) is computed for the selected operating mode and its neighboring modes to analyze the mode competition (Fig. 1). The start oscillation current can be calculated in a linearized single-mode theory and described in detail elsewhere [24]. All the modes lie in amplification band $\Delta\omega = \pi/T$ (T is the transient time of the electrons through the resonator) are considered in the start oscillation current calculation [25]. From the inspection of the SOC curves, it is clear that $TE_{4,4}$ is the most probable competing mode for the selected operating mode as the optimum operation point is found in the hard excitation region.

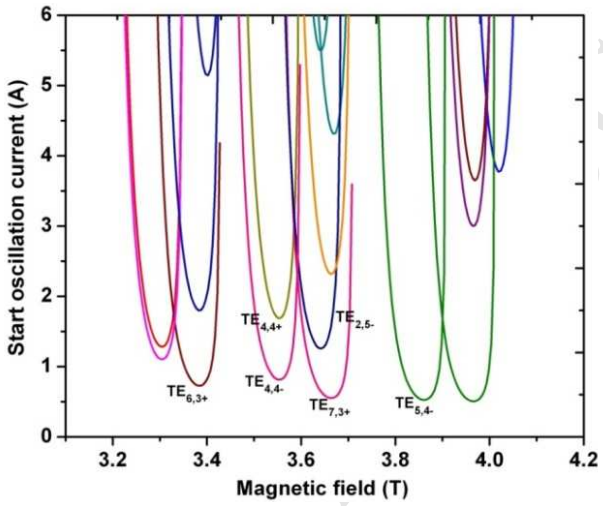

FIG. 1 Start oscillation current as a function of magnetic field for various modes (V_b=52 kV, I_b=7 A, α=1.35, R_c=8.2 mm, R_b=3.75 mm)

A simple cylindrical open resonator type of interaction cavity is considered here, which is a standard three section structure with an input taper section, a uniform midsection and an output taper section. For the selected operating mode, the cavity radius and beam radius are 8.25 mm and 3.75 mm, respectively. The gyrotron interaction cavity is a moderate Q structure (generally 500 to 1500) and thus the middle section length (L) is considered between 5λ to 7λ ($Q_d \sim L^2$). Table 3 shows the variation of diffractive Q value and resonant frequency with middle section length for the operating mode $TE_{7,3}$. The midsection length of 20 mm corresponding to Q_d=776 is finally selected because the Ohmic wall loading becomes high for larger Q values. The total Q (Q_{tot}) value can be given as $1/Q_{tot}=1/Q_d+1/Q_{ohm}$, where Q_{ohm} is the ohmic quality factor. The calculated value of Q_{ohm} for the designed interaction cavity is 18000 considering the electrical conductivity of oxygen free high conductivity copper as the cavity material ($\sigma = 5.7*10^7$ S/m). The Gaussian type of electric field profile is optimized for the various values of input taper (θ_1) and output taper (θ_2) angles. Fig. 2 shows the Gaussian type of electric field profile for the

finally optimized interaction cavity geometry. Final optimized design values of cold cavity are given in table 4.

Table 3: Diffractive Q value and resonant frequency for various cavity lengths

L (mm)	f (GHz)	Q_d
16	94.263	500
18	94.210	630
20	94.192	776
22	94.182	938
24	94.150	1117

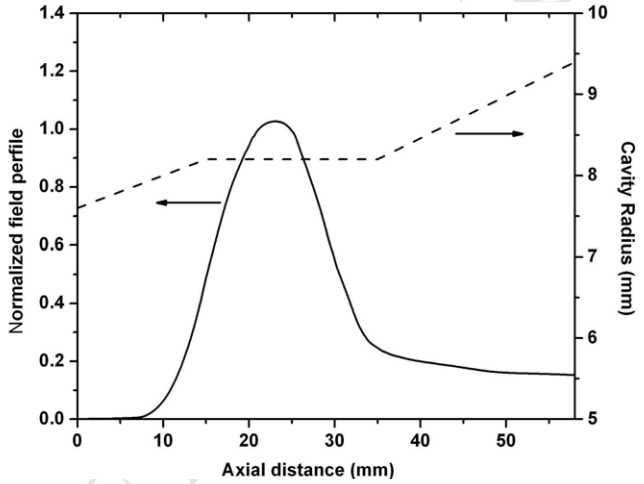

FIG 2 Normalized cold cavity field profile along the cavity length

Table 4: Final cold cavity design values

Cavity radius (R_c)	8.25 mm
Beam radius (R_b)	3.758 mm
Middle section length (L)	20 mm
Input taper length (L_1)	15 mm
Output taper length (L_2)	23 mm
Input taper angle (θ_1)	2.3^0
Output taper angle (θ_2)	3^0

3. BEAM WAVE INTERACTION COMPUTATION

The beam-wave interaction simulations are performed for the interaction cavity geometry obtained from the cold cavity design. The PIC code MAGIC and an in-house developed code are used in the

beam-wave interaction calculations. The developed code is based on the self consistent generalized non linear equations described in detail in Refs. [13,14] and is used for the calculations of efficiency, output power and optimization of beam parameters. The coupled generalized equations are given as:

$$\frac{du}{d\zeta} = 2Ff(\zeta)(1-u)^{n/2}\sin\theta \qquad (1)$$

$$\frac{d\theta}{d\zeta} = \Delta - u - nFf(\zeta)(1-u)^{n/2-1}\cos\theta \qquad (2)$$

where u, θ, F, ζ, Δ are normalized energy, electron phase, normalized field amplitude, normalized axial position and detuning factor, respectively. The normalized field amplitude and detuning factor are given as:

$$F = \frac{E_0}{B_0}\beta_{\perp 0}^{(n-4)}\left(\frac{n^{n-1`}}{n!}\right)J_{m\pm n}\left(k_\perp R_b\right) \qquad (3)$$

$$\Delta = \frac{2}{\beta_{\perp 0}^2}\left(1-\frac{n\Omega_c}{\omega}\right) \qquad (4)$$

where E_0, B_0, $\beta_{\perp 0}$, Ω_c, ω, n are the electric field intensity, static magnetic field at cavity, normalized perpendicular velocity of electrons, electron cyclotron frequency and angular frequency of RF, respectively. The calculations are performed considering the Gaussian type of field profile and the integration is performed in the limit of $-\sqrt{3}\mu/2 \le \zeta \le \sqrt{3}\mu/2$. The normalized interaction cavity length (μ) is given as:

$$\mu = \pi\frac{\beta_{\perp 0}^2}{\beta_{z0}}\frac{L}{\lambda} \qquad (5)$$

where β_{z0}, L and λ are normalized axial velocity of electrons, cavity length and free space wavelength, respectively. The total interaction efficiency can be given as:

$$\eta = \frac{\beta_{\perp 0}^2}{2\left(1-\gamma_0^{-1}\right)}\eta_\perp \qquad (6)$$

where γ_0 is the relativistic factor at the cavity entrance.

Further, perpendicular interaction efficiency $\eta_\perp$ is defined as:

$$\eta_\perp(F,\mu,\Delta) = \left\langle u(\zeta_{out})\right\rangle_{\theta_0} \qquad (7)$$

here bracket denotes the average of particles energy at the end of interaction cavity.

The beam-wave interaction computation is performed by using both the codes (3D Particle in Cell-MAGIC and in-house developed code based on equations from (1) to (7)). MAGIC-3D is a user-configurable code that self-consistently solves the full set of time dependent Maxwell's equations and

the complete Lorentz force equation to provide the interaction between the space charge and electromagnetic fields. A variety of 3D algorithms are available for problem-specific solutions. We have used the Maxwell CENTERED algorithm (specific for relativistic problems such as gyrotron) in the cylindrical coordinate system for the modeling of the resonant structure. The electron beam parameters are optimized considering the goal of maximum interaction efficiency at the desired frequency and summarized in table 5. Figs. 3-8 show the results of beam-wave interaction computations. Fig. 3 shows the result of growth of beam wave interaction efficiency along with the cavity length. The analytical and simulated results show very good similarity with approximately 37% interaction efficiency. Figs. 4 and 5 show the simulated as well as analytical results of efficiency variation with respect to the beam current and magnetic field, respectively. Fig. 6 shows the result of electron beam bunching obtained by MAGIC simulations. The snapshots of the electron beamlets are taken just when the beam enters into the cavity (Fig. 6a) and after the beam wave interaction at 300 ns (Fig. 6b). Figure clearly represents the efficient electron beam bunching during the beam wave interaction. Fig. 7 shows the frequency spectrum which is found through the Fast Fourier Transform (FFT) of the time history of the fields. The frequency spectrum shows a sharp peak of electric field gain at 94.6 GHz, which is the frequency at the operating mode $TE_{7,3}$. There are no other peaks around the frequency of 94.6 GHz, which clearly indicate the suppression of competing modes around the operating frequency of 95 GHz. Some small peaks also appear in the frequency spectrum, which indicates the weak growth of parasitic oscillations. Fig. 8 shows the typical plots of MAGIC simulations representing the power and frequency growth with respect to time. The power and frequency growths become stable around 150 ns. The simulation results confirm more than 100 kW power with 37 % interaction efficiency at $TE_{7,3}$ mode.

Table 5: Optimized electron beam parameters

Beam current (I_b)	7 A
Beam voltage (V_b)	52 kV
Magnetic field at cavity (B_0)	3.56 T
Velocity ratio (α)	1.35
Beam radius (R_b)	3.75 mm

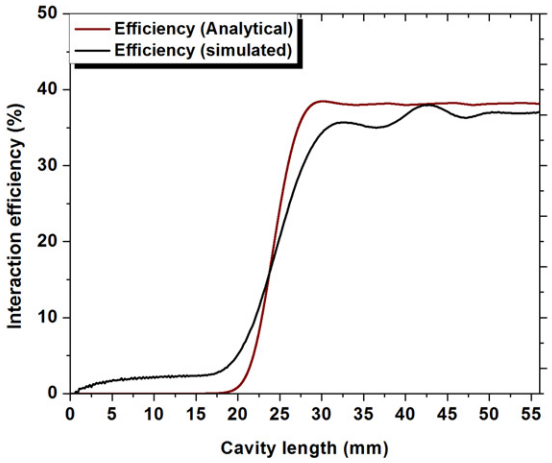

FIG 3 Growth of interaction efficiency along with the cavity length (V_b= 52 kV, I_b= 7 A, α= 1.35, B_0= 3.56 T)

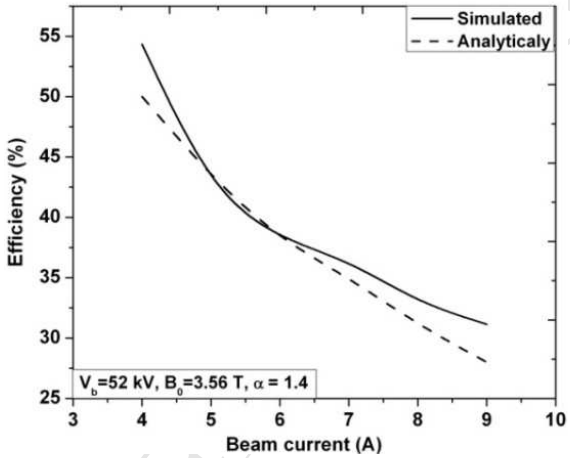

FIG 4 Efficiency as the function of beam current (V_b= 52 kV, α= 1.35, B_0= 3.56 T)

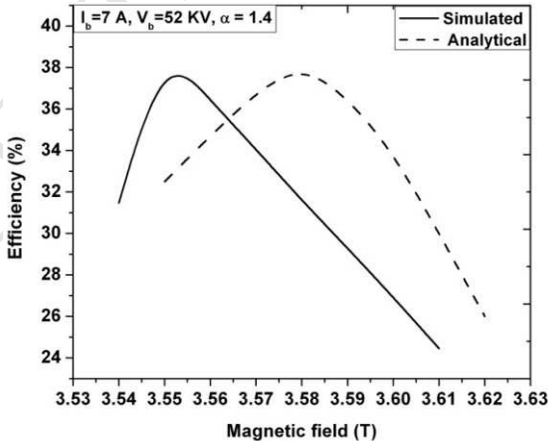

FIG 5 Efficiency as the function of beam voltage (V_b= 52 kV, I_b= 7 A, α= 1.35)

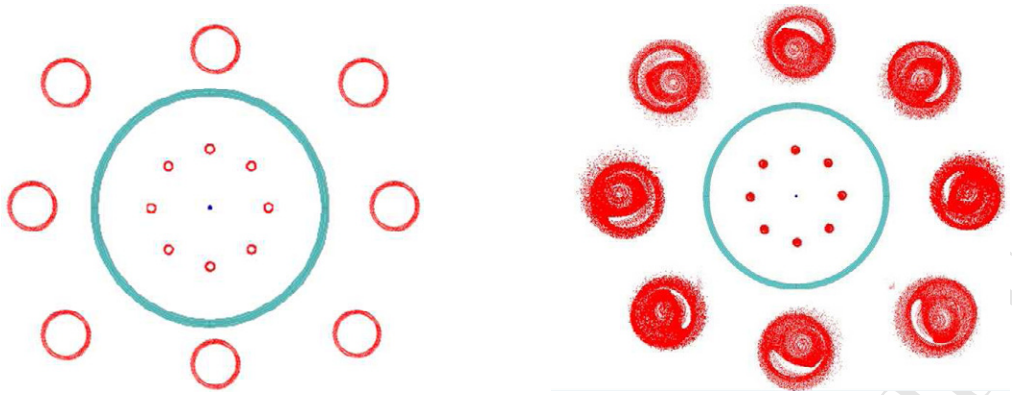

(a) **(b)**

FIG 6 Electron beamlets in the interaction cavity **(a)** before the interaction **(b)** after the interaction (at 300 ns)

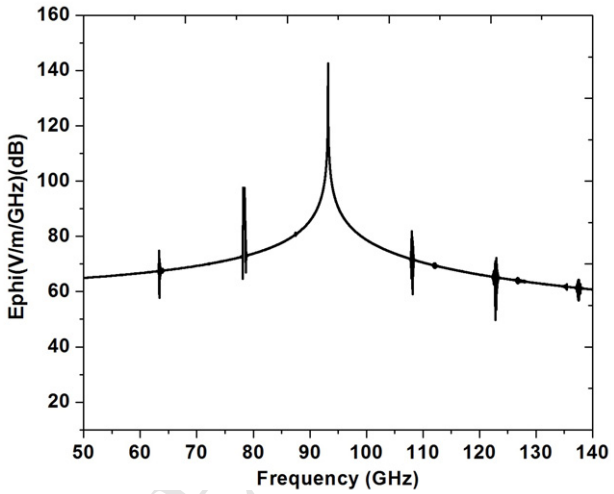

FIG 7 Frequency spectrum (V_b= 52 kV, I_b= 7 A, α= 1.35, B_0= 3.56 T)

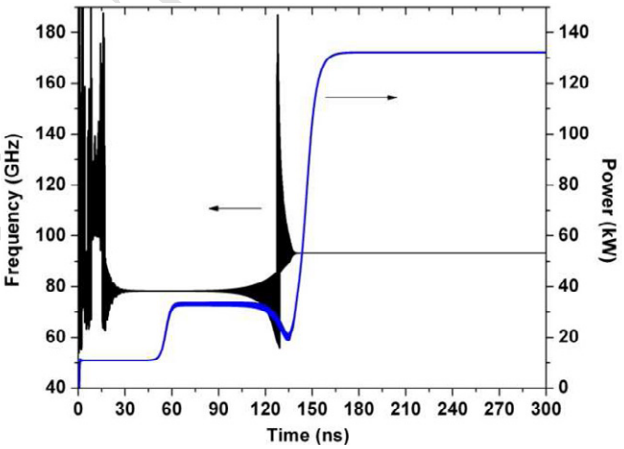

FIG 8 Frequency and power growth with respect to time (V_b= 52 kV, I_b= 7 A, α= 1.35, B_0= 3.56 T)

4. MAGNETRON INJECTION GUN

The interaction cavity simulation results give the optimum values of electron beam parameters according to the requirement of output power and efficiency. Considering the electron beam parameters given in table 5, a triode type MIG (magnetron injection gun) is designed. A triode type MIG is chosen over diode type as it provides better control on the beam properties. The initial gun parameters such as cathode angle, cathode radius, cathode anode gap, cathode slant length, etc are obtained from the analytical trade-off equations [26-28]. Optimization of the MIG geometry is performed by using the commercially available code EGUN [29] and the in-house developed code MIGANS [30, 31]. MIGANS is basically a post processor of the EGUN code and used to find out the electron beam parameters, like, α (= $\beta_\perp/\beta_z$), the maximum transverse velocity spread ($\delta\beta_{\perp max}$), the larmor radius (r_l), and beam radius (R_b). Here, $\beta_\perp$ and β_z are the average transverse and axial electron velocities, respectively in the interaction region normalized to the speed of light (c). The main goals of the MIG design are the launching of electron beam at particular radial position (R_b=3.75 mm) with minimum velocity spread ($\delta\beta_{\perp max}$<5%) and an optimum velocity ratio ($\alpha \approx 1.35$). Considering these goals, the geometry of the cathode (emitter) and anodes, gap between cathode and anodes, slant angle and slant length of cathode, magnetic field profile, magnetic field at cathode center, modulating anode voltage, etc are optimized. The Gaussian type of magnetic field profile with peak value at interaction cavity center is required to obtain the adiabatic compression in the electron beam [16], so that an optimum value of velocity ratio (α) can be achieved. The optimum magnetic field profile is given in Fig. 9 including the cathode position and interaction cavity center position. Further, the electron beam trajectory simulations are performed by using the EGUN code. Fig. 10 shows the optimized MIG geometry and electron beam profile. Table 6 shows the optimized values of beam parameters and MIG geometry obtained by EGUN simulations.

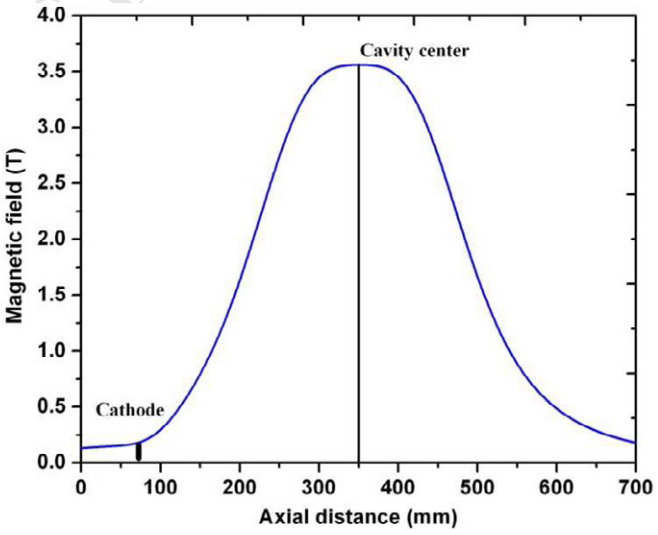

FIG 9 Magnetic field profile including cavity and cathode position

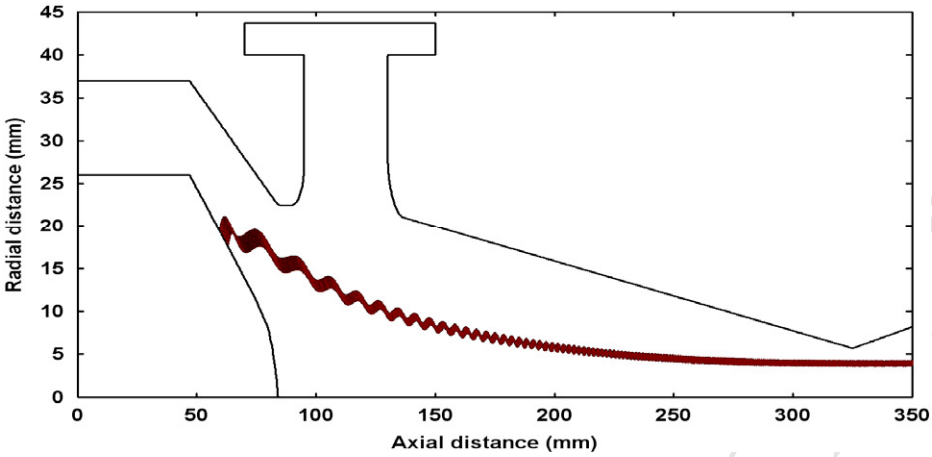

FIG 10 Electron beam trajectory with MIG geometry

Table 6 Optimized beam parameters and MIG geometry

Beam voltage (V_b)	52 kV
Beam current (I_b)	7A
Modulating anode voltage (V_a)	39 kV
Transverse velocity spread (($\delta\beta_\perp$)	1.11%
Velocity ratio (α)	1.36
Larmor radius (r_l)	0.17 mm
Cathode magnetic field (B_c)	0.1374 T
Cavity magnetic field	3.56 T
Average beam radius (R_b)	3.8 mm
Cathode current density (J_c)	1.5 A/cm^2
Cathode slant length (ϕ_c)	3.9 mm
Cathode radius (r_c)	18.46 mm
Slant angle	28 degree

It is very difficult to maintain the MIG operating parameters fixed during the fabrication and operation of the device. A small change in the MIG parameters affects the beam-wave interaction which leads to the change in output power. The MIG parameters, namely modulating anode voltage and cathode magnetic field, affect the beam quality parameters (velocity ratio and velocity spread) critically [16]. Fig. 11 and 12 show the effect of modulating anode voltage and cathode magnetic field on the beam quality parameters.

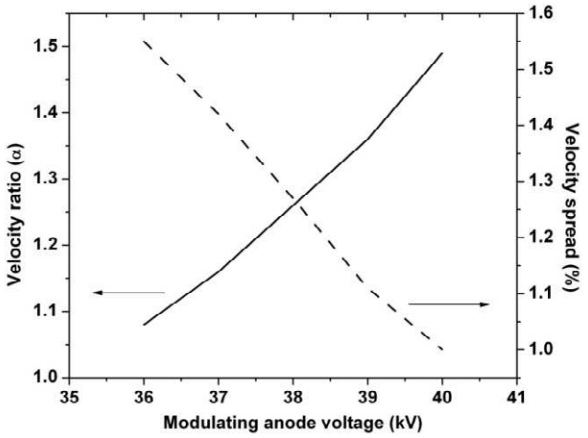

FIG 11 Velocity ratio and spread with respect to modulating anode voltage. Fixed parameters are V_b=52 kV, I_b=7 A, B_c=1374 Gauss, B_0= 3.56 T

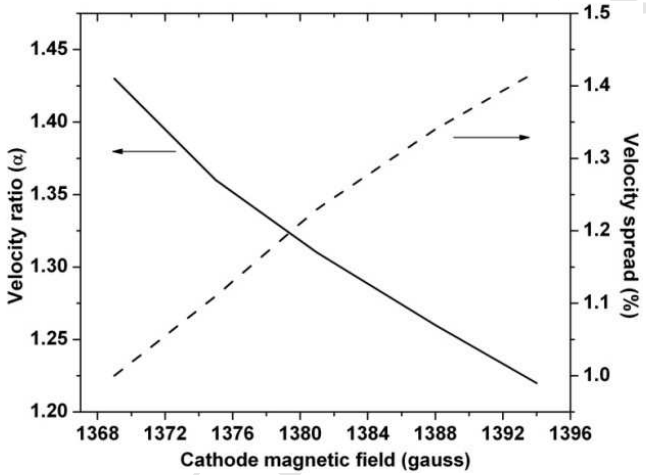

FIG 12 Velocity ratio and spread with respect to cathode magnetic field. Fixed parameters are V_b=52 kV, I_b=7 A, V_a=39 kV, B_0= 3.56 T

5. BEAM TUNNEL

The beam tunnel connects the interaction cavity with the magnetron injection gun. The magnetic field is highly inhomogeneous inside the beam tunnel and thus pure metallic structure can support the parasitic oscillation which further degrades the beam quality. To suppress the parasitic oscillations, the beam tunnel is specially designed by using the periodic arrangement of copper rings and highly lossy ceramic rings. Highly lossy ceramic rings are also used to absorb the RF signal, somehow propagates from the interaction cavity to electron gun. AlN-SiC is used as the ceramic material due to its very good lossy properties (ε_r= 15, $tan\delta$= 0.25). The design of the beam tunnel for 95 GHz gyrotron is performed by using the design methodology as used previously for 42 GHz gyrotron and discussed in detail in Refs. [32-34]. CST-Microwave Studio is used in the beam tunnel design and parasitic mode oscillation analysis. As mentioned in Ref. [34], the symmetric TE modes exhibit very high probability of excitation

in the beam tunnel during the electron beam transportation and thus the symmetric modes up to $TE_{0,10}$ are analyzed in detail by using various methods described in [33-35]. To analyze the backward beam-wave interaction, the dispersion curves are studied for all the symmetric modes and the copper rings towards the cavity side of beam tunnel. The S matrix simulations are performed for the designed structure by using the CST-Microwave Studio and the results show 95.5 % absorption, 4.5 % reflection and approximately 0 % transmission of RF. Final designed beam tunnel structure is shown in Fig. 13, which exhibits almost no parasitic mode oscillations.

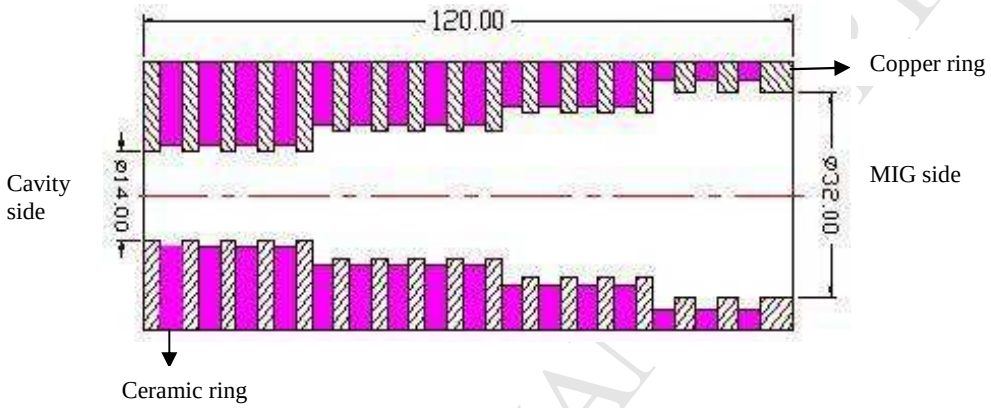

FIG 13 Designed beam tunnel (all dimensions are in millimeter)

6. COLLECTOR AND RF WINDOW

The beam-wave interaction simulation results show around 130 kW power from 364 kW beam power is transferred to the RF. The spent electron beam is collected in a cylindrical waveguide type of structure called collector. Single-stage depressed collector (SDC) is designed for 95 GHz gyrotron to enhance the overall tube efficiency (up to 50%) and to minimize the thermal loading on the collector wall [36, 37]. In depressed collectors, the remaining kinetic energy of the spent electron beam is partly converted into the electrical energy and thus reducing the power consumption of the tube, which otherwise would heat up the collector surface [36, 37]. To convert the electron beam kinetic energy into the electrical energy, the potential on the surface of the depressed collector, on which the beam is collected, is decreased toward the cathode potential. The efficiency of depressed collector is given as $\eta_{coll} = P_{coll}/(P_{beam}-P_{RF})$, where P_{coll} is the power recovered by the depressed collector, P_{beam} and P_{RF} are the electron beam power and the generated RF power. Further, $P_{coll}=U_{coll}.I_{coll}$ with U_{coll} is the applied collector voltage and I_{coll} is the collector current. The design of SDC is completed by using the trajectory code EGUN considering two design goals: (1) maximum spread in electron beam at the collector wall, (2) maximum collector efficiency. Rigorous simulations are performed to achieve optimum beam spread and collector efficiency. Extra three collector magnet coils are used to spread out the electron beam at the collector

surface. The position of magnet coils and number of turns are optimized for maximum beam spreading at the collector wall and given in Table 7. Each magnet consist two layers having same ampere turns. Fig. 14 shows the electron beam spreading including collector geometry and magnetic field profile. An almost uniform spreading of 308.5 mm is achieved as shown in Fig. 14. The calculated heat flux for this spreading is 0.131 kW/cm^2, which is under the technical limit of OFHC copper (1 kW/cm^2) [38]. The optimized depressed potential applied on the collector is 22.5 kV, which enhance the overall tube efficiency up to more than 50 % (collector efficiency is 66.5 %). The secondary electron emission analysis is very important and critical for MW gyrotrons due to very high spent electron beam power. Here, the spent electron beam power is not as higher as in case of MW gyrotron and thus the analysis of secondary electron emission not performed at this stage.

Table 7 Positions and ampere turns of magnet coils at collector

	Radial position (mm)		**Axial position (mm)**	**Ampere turns**
	Layer 1	**Layer 2**		
Magnet 1	105	115	900	585
Magnet 2	105	115	1044	390
Magnet 3	105	115	1190	600

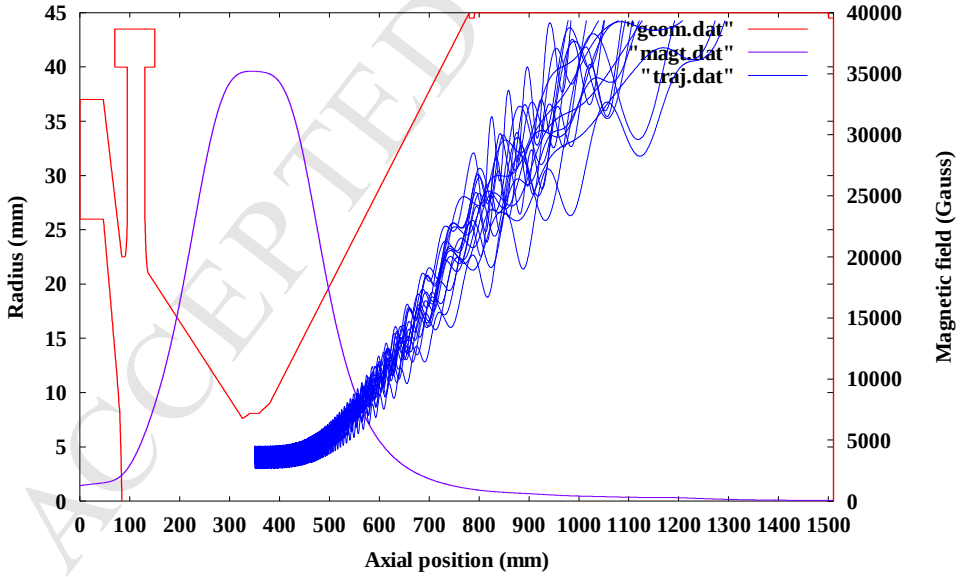

FIG 14 Electron beam spreading at collector wall including magnetic field profile and collector geometry

The RF window is a critical part of any microwave tube that transmits the RF power to the external system. The window material must exhibit high mechanical strength, low RF loss and good thermal

stability. Considering these technical issues, several materials are explored by the gyrotron community and discussed in detail in Refs. [3, 39]. For the present design, CVD diamond is selected as the window material due to its excellent thermal, mechanical and dielectric properties [40]. The CVD diamond also provides good compatibility with the brazing and metallization process. Due to the very good thermal conductivity of CVD diamond and very weak dependency of the electrical parameters on temperature, edge cooled single disk design is selected for this gyrotron. The optimized disk thickness and radius are shown in table 8. The design tool CST-Microwave Studio is used in the transient analysis of CVD diamond window. Fig. 15 shows the simulation results for the optimized geometry given in table 8. The transmission more than 99 % is achieved for the designed RF window.

Table 8 Geometry and dielectric properties of RF window [3]

Disk thickness	1.988 mm
Disk radius	45 mm
Loss tangent	$2x10^{-5}$
Permittivity	5.67

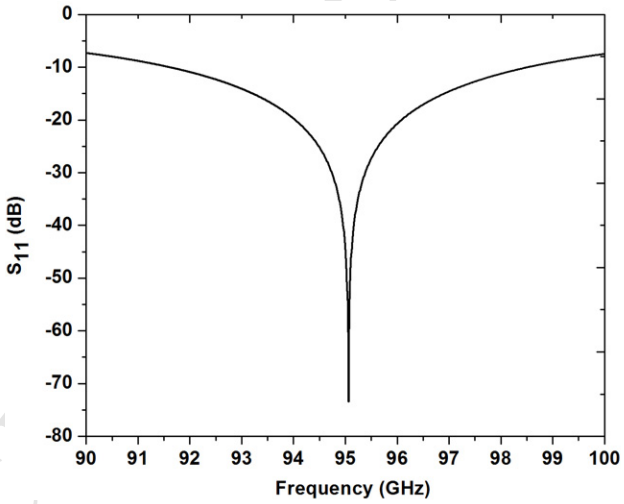

FIG 15 S_{11} with respect to frequency

7. CONCLUSION

The design of 95 GHz, 100 kW gyrotron operating at $TE_{7,3}$ mode for ADS application is presented in this manuscript. Conventional cylindrical cavity, triode type MIG and single stage depressed collector are considered for this gyrotron. A beam-wave interaction computation code based on the generalized non-linear theory is also developed and used here in the efficiency calculation. The results obtained from the in-house developed code and PIC code MAGIC show good similarity. The design results show more

than 100 kW RF power with 37 % interaction efficiency. The collector efficiency (66.5 %) enhances the overall tube efficiency up to 50 %.

Acknowledgement

The authors are pleased to acknowledge the support of Dr. Chandra Shekhar, Director, CEERI Pilani and Dr. SN Joshi, National Coordinator of Gyrotron project. The authors also wish to thank to the team members of gyrotron for helpful discussions.

REFERENCES

[1] G. Dammertz, "Vacuum requirements in high power microwave tubes", *Vacuum*, vol. 46, pp. 785, 1995.

[2] G. Faillon, "Technical and industrial overview of RF and microwave tubes for fusion", *Fusion Engineering and Design*, vol. 46, pp. 371, 1999.

[3] M. Thumm, State-of-the-art of high power gyro-devices and free electron masers update 2006, Forschungszentrum Karlsruhe, Karlsruhe, Germany, Scientific Report FZKA 7289, February 2007.

[4] M. Thumm, "High power gyro-devices for plasma heating and other applications", *Int. J. of Infrared and Millimeter Waves*, vol. 26, pp. 483, 2005.

[5] N. Kumar, U. Singh, T. P. Singh, A. K. Sinha, "A review on the applications of high power, high frequency microwave source: Gyrotron", *J. Fusion Energy*, vol. 30, pp. 257, 2011

[6] M. Thumm, "Novel applications of millimeter and sub-millimeter wave gyro-devices", *Int. J. Infrared Millimeter Terahertz Wave*, vol. 22, pp. 377, 2001.

[7] A. V. Gaponov-Grekhov, V. L. Granatstein, *Application of High Power Microwaves*, Artech House Publication, London, 1994.

[8] S. LeVine, The Active Denial System A Revolutionary, Nonlethal Weapon for Today's Battlefield, Technical Report, Center for Technology and National Security Policy (National Defense University, Washington DC, 2009).

[9] H. J. Liebe, MPM—an atmospheric millimeter-wave propagation model, "*Int. J. Infrared and Millimeter Wave*" vol. 10, pp. 631, 1989.

[10] J. Neilson, M. Read, L. Ives. Design of a permanent magnet gyrotron for active denial systems, Proc. IEEE-IVEC, pp. 92, Rome, 2009

[11] www.cpii.com

[12] MAGIC User Mannual: 2007 version of Magic 3D, ATK Mission Research, Washington.

[13] B. G. Danly and R. J. Temkin, "Generalized nonlinear harmonic gyrotron theory", *Physics of Fluids*, vol. 29, pp. 561-567, 1986.

[14] N.S Ginzburg and G.S. Nusinovich, "On the nonlinear theory of a relativistic gyrotron", Izv. Vuzov. Radiofizika. vol. 22, pp. 754-763, 1979.

[15] A. K. Ganguli, and K. R. Chu, "Limiting current in gyrotrons", *J. Infrared Milli. Terahz. Waves*, vol. 5, pp. 103, 1984.

[16] C. J. Edgecombe, *Gyrotron Oscillators: Their Principles and Practice* ,Taylor & Francis, London, 1993, pp. 240

[17] K. A. Avramides, O. Dumbrajs, S. Kern, I. Gr. Pagonakis, and J. L. Vomvoridis, 35th EPS Conference on Plasma Phys., pp. 4.105, Hersonissos, June 2008.

[18] N. Kumar, U. Singh, A. Kumar, H. Khatun and A. K. Sinha, "On the design of high efficiency double beam gyrotron", *IEEE Tr. Plasma Science*, vol. 39, pp. 1781-1785, 2011.

[19] N. Kumar, U. Singh, A. Kumar, H. Khatun, T.P. Singh and A.K. Sinha, "Design of 35 GHz Gyrotron for Material Processing Applications", *Progress in Electromagnetic Research B (PIER B)*, vol. 27, pp. 273-288, 2011.

[20] G.S. Nusinovich, Introduction to the physics of gyrotron, Johns Hopkins Univ. Press, Baltimore MD, 2004, pp. 58.

[21] G. Nusinovich, "Mode interaction in gyrotrons", *Int. J. Electronics*, vol. 51, pp. 457-474, 1981.

[22] B. Levush and T.M. Antonsen Jr., "Mode Competition and Control in High-Power Gyrotron Oscillators", *IEEE Tr. Plasma Science*, vol. 18, pp. 260-272, 1990

[23] D. R. Whaley, M. Q. Tran, T. M. Tran, and T. M. Antonsen Jr., "Mode Competition and Startup in Cylindrical Cavity Gyrotrons Using High-Order Operating Modes", *IEEE Tr. Plasma Science*, vol. 22, pp. 850-860, 1994.

[24] E. Borie, and B. Jodicke, "Comments on the linear theory of the gyrotron", *IEEE Trans. Plasma Sci.*, vol. 16, pp. 116-121, 1988.

[25] R.A Correa, A.B. Levush and T.M Antonsen, "High efficiency cavity design of a 170 GHz gyrotron for fusion applications", *Physics of Plasmas*, vol. 4, pp. 209-216, 1997.

[26] J. M. Baird and W. Lawson, "Magnetron injection gun (MIG) design for gyrotron applications", *Int. J. Electronics*, vol. 61, pp. 953-967, 1986.

[27] W. Lawson, "MIG Scaling", *IEEE Trans. Plasma Science*, vol. 16, pp. 290-295, 1988.

[28] U. Singh, A. Bera, R.R. Rao and A.K. Sinha, "Synthesized Parameters of MIG for 200 kW, 42 GHz Gyrotron" *J. of Infrared, Millimeter, and Terahertz Waves*, vol. 31, pp. 533-541, 2009.

[29] EGUN, *Hermannsfeldt, W.B., 1979, Stanford Linear Accelerator Center*, Stanford University Report SLAC-226.

[30] U. Singh, A. Bera, N. Kumar and A.K. Sinha, "Numerical Simulation of MIG for 200 kW, 42 GHz Gyrotron", *Int. J. of Infrared and millimeter Waves*, vol. 31, pp. 708-713, 2010.

[31] U. Singh, N. Kumar, N. Kumar, S. Tandon, H. Khatun, LP Purohit and AK Sinha, "Numerical simulation of MIG for 120 GHz, 1MW gyrotron", *Progress in Electromagnetic Research Letters*, Vol. 16, pp. 21-34, 2010.

[32] N. Kumar, M.K. Alaria, U. Singh, A. Bera, T.P. Singh and A.K. Sinha, "Design of beam tunnel for 42 GHz, 200 kW gyrotron", *Int. J. of Infrared and millimeter Waves*, vol. 31, pp. 601-607, 2010.

[33] N. Kumar, U. Singh, T.P. Singh and A.K. Sinha, "Analysis of parasitic oscillations in 42 GHz gyrotron beam tunnel", *Int. J. electronics*, vol. 98, pp. 271-277, 2011.

[34] N. Kumar, U. Singh, T.P. Singh and A.K. Sinha, "Suppression criteria of parasitic mode oscillations in gyrotron beam tunnel", vol. 18, pp. 022507, 2011.

[35] G. Gantenbein, G. Dammertz, J. Flamm, S. Illy, S. Kern, G. Latsas, B. Piosczyk, T. Rzesnicki, A. Samartsev, A. Schlaich, M. Thumm, and I. Tigelis, "Experimental Investigations and Analysis of Parasitic RF Oscillations in High-Power Gyrotrons", *IEEE Trans. Plasma Sci.*, vol. 380, pp. 1168-1177, 2010.

[36] M.E. Read, W.G. Lawson, A.J. Dudas and A. Singh, "Depressed Collectors for High-Power Gyrotrons", *IEEE Tr. Electron Devices*, vol. 37, pp. 1579-1589, 1990.

[37] B. Piosczyk, C. T. Iatrou, G. Dammertz, and M. Thumm, "Single-Stage Depressed Collectors for Gyrotrons", *IEEE Tr. Plasma Science*, vol. 24, pp. 579-585, 1996.

[38] G.S. Nusinovich, *Introduction to the Physics of Gyrotron*. Johns Hopkins Univ. press, Baltimore, MD, 2004.

[39] M. Thumm, "Development of output power window for high power long pulse gyrotrons and EC wave applications", *Int. J. Infrared Milli. Waves*, vol. 19, pp. 3-14, 1998.

[40] R. Heidinger, G. Dammertz, A. Meier and M. Thumm, "CVD diamond windows studied with low and high power millimeter waves", *IEEE Trans. Plasma Sci.*, vol. 30,pp. 800-807,2002.